The Astrophysical Journal Letters, 983:L36 (13pp), 2025 April 20 https://doi.org/10.3847/2041-8213/adadd7

TOI-6324 b: An Earth-mass Ultra-short-period Planet Transiting a Nearby M Dwarf

Rena A. Lee[1,36], Fei Dai[1,2,3], Andrew W. Howard[3], Samuel Halverson[4], Jonathan Gomez Barrientos[2], Michael Greklek-McKeon[2], Heather A. Knutson[2], Benjamin J. Fulton[3], Guðmundur Stefánsson[5], Jack Lubin[6], Howard Isaacson[7,8], Casey L. Brinkman[1,36], Nicholas Saunders[1,36], Daniel Hey[1], Daniel Huber[1], Lauren M. Weiss[9], Leslie A. Rogers[10], Diana Valencia[11], Mykhaylo Plotnykov[12], Kimberly Paragas[2], Renyu Hu[4,2], Te Han[13], Erik A. Petigura[6], Ryan Rubenzahl[14], David R. Ciardi[15], Aaron Householder[16,17], Gregory J. Gilbert[6], J. M. Joel Ong[1,37], Jingwen Zhang[1,38], Jacob Luhn[4], Luke Handley[3], Corey Beard[13,38], Steven Giacalone[3], Rae Holcomb[13], Judah Van Zandt[6], Ashley D. Baker[18], Max Brodheim[19], Matt Brown[19], David Charbonneau[20], Karen A. Collins[20], Ian J. M. Crossfield[21], William Deich[22], Xavier Dumusque[23], Steven R. Gibson[18], Emily Gilbert[4], Grant M. Hill[19], Bradford Holden[22], Jon M. Jenkins[24], Stephen Kaye[18], Russ R. Laher[15], Kyle Lanclos[19], W. Garett Levine[25], Joel Payne[19], Alex S. Polanski[21,26], John O'Meara[19], George R. Ricker[17], Kodi Rider[27], Paul Robertson[13], Arpita Roy[28], Joshua E. Schlieder[29], Christian Schwab[30], Sara Seager[16,17,31], Abby P. Shaum[3], Martin M. Sirk[27], Stephanie Striegel[32,24], Johanna Teske[33], John Valliant[19], Roland Vanderspek[17], Gautam Vasisht[4], Josh Walawender[19], Sharon Xuesong Wang[34], Joshua N. Winn[35], Edward Wishnow[27], and Sherry Yeh[19]

[1] Institute for Astronomy, University of Hawai'i, 2680 Woodlawn Drive, Honolulu, HI 96822, USA; renaalee@hawaii.edu
[2] Division of Geological and Planetary Sciences, 1200 E California Boulevard, Pasadena, CA 91125, USA
[3] Department of Astronomy, California Institute of Technology, Pasadena, CA 91125, USA
[4] Jet Propulsion Laboratory, California Institute of Technology, 4800 Oak Grove Drive, Pasadena, CA 91109, USA
[5] Anton Pannekoek Institute for Astronomy, University of Amsterdam, Science Park 904, 1098 XH Amsterdam, The Netherlands
[6] Department of Physics & Astronomy, University of California Los Angeles, Los Angeles, CA 90095, USA
[7] Department of Astronomy, 501 Campbell Hall, University of California, Berkeley, CA 94720, USA
[8] Centre for Astrophysics, University of Southern Queensland, Toowoomba, QLD, Australia
[9] Department of Physics and Astronomy, University of Notre Dame, Notre Dame, IN 46556, USA
[10] Department of Astronomy & Astrophysics, University of Chicago, 5640 S Ellis Avenue, Chicago, IL 60637, USA
[11] Centre for Planetary Sciences, University of Toronto, 1265 Military Trail, Toronto, ON, M1C 1A4, Canada
[12] Department of Physics, University of Toronto, Toronto, ON M5S 3H4, Canada
[13] Department of Physics & Astronomy, The University of California, Irvine, Irvine, CA 92697, USA
[14] Center for Computational Astrophysics, Flatiron Institute, 162 Fifth Avenue, New York, NY 10010, USA
[15] NASA Exoplanet Science Institute/Caltech-IPAC, California Institute of Technology, Pasadena, CA 91125, USA
[16] Department of Earth, Atmospheric, and Planetary Sciences, Massachusetts Institute of Technology, Cambridge, MA 02139, USA
[17] Department of Physics and Kavli Institute for Astrophysics and Space Research, Massachusetts Institute of Technology, Cambridge, MA 02139, USA
[18] Caltech Optical Observatories, California Institute of Technology, Pasadena, CA 91125, USA
[19] W. M. Keck Observatory, 65-1120 Mamalahoa Highway, Kamuela, HI 96743, USA
[20] Center for Astrophysics, Harvard & Smithsonian, 60 Garden Street, Cambridge, MA 02138, USA
[21] Department of Physics & Astronomy, University of Kansas, 1082 Malott,1251 Wescoe Hall Drive, Lawrence, KS 66045, USA
[22] UC Observatories, University of California, Santa Cruz, CA 95064, USA
[23] Observatoire Astronomique de l'Université de Genève, Chemin Pegasi 51, 1290 Versoix, Switzerland
[24] NASA Ames Research Center, Moffett Field, CA 94035, USA
[25] Department of Astronomy, Yale University, New Haven, CT 06511, USA
[26] Lowell Observatory, 1400 W Mars Hill Road, Flagstaff, AZ 86001, USA
[27] Space Sciences Laboratory, University of California, Berkeley, CA 94720, USA
[28] Astrophysics & Space Institute, Schmidt Sciences, New York, NY 10011, USA
[29] NASA's Goddard Space Flight Center, Greenbelt, MD 20771, USA
[30] School of Mathematical and Physical Sciences, Macquarie University, Balaclava Road, North Ryde, NSW 2109, Australia
[31] Department of Aeronautics and Astronautics, Massachusetts Institute of Technology, Cambridge, MA 02139, USA
[32] SETI Institute, Mountain View, CA 94043, USA
[33] Earth and Planets Laboratory, Carnegie Institution for Science, 5241 Broad Branch Road, NW, Washington, DC 20015, USA
[34] Department of Astronomy, Tsinghua University, Beijing 100084, People's Republic of China
[35] Department of Astrophysical Sciences, Princeton University, 4 Ivy Lane, Princeton, NJ 08540, USA
Received 2024 November 6; revised 2024 December 27; accepted 2025 January 5; published 2025 April 16

Abstract

We report the confirmation of TOI-6324 b, an Earth-sized ($1.059 \pm 0.041\ R_{\oplus}$) ultra-short-period (USP) planet orbiting a nearby (∼20 pc) M dwarf. Using the newly commissioned Keck Planet Finder spectrograph, we have measured the mass of TOI-6324 b $1.17 \pm 0.22\ M_{\oplus}$. Because of its extremely short orbit of just ∼6.7 hr, TOI-6324

[36] NSF Graduate Research Fellow.
[37] NASA Hubble Fellow.
[38] NASA FINESST Fellow.

b is intensely irradiated by its M dwarf host and is expected to be stripped of any thick H/He envelope. We were able to constrain its interior composition and found an iron-core mass fraction (CMF = 27% ± 37%) consistent with that of Earth (∼33%) and other confirmed USPs. TOI-6324 b is the closest to an Earth-sized USP confirmed to date. TOI-6324 b is a promising target for JWST phase-curve and secondary eclipse observations (emission spectroscopy metric = 25), which may reveal its surface mineralogy, day–night temperature contrast, and possible tidal deformation. From seven sectors of TESS data, we report a tentative detection of the optical phase-curve variation with an amplitude of 42 ± 28 ppm.

Unified Astronomy Thesaurus concepts: Exoplanet structure (495); Exoplanets (498); Radial velocity (1332); Exoplanet astronomy (486)

Materials only available in the online version of record: machine-readable table

1. Introduction

Detecting and characterizing Earth-like planets is a leading pursuit in the field of exoplanetary astronomy. Photometric surveys, such as the Transiting Exoplanet Survey Satellite (TESS) mission (G. R. Ricker et al. 2015), have enabled the identification of hundreds of Earth-sized planets and planet candidates. To begin to explore the interiors of these distant worlds, we require precise mass and radius measurements. However, true Earth analogs, with radial-velocity (RV) semiamplitudes on the order of $\sim$10 cm s^{-1}, are not yet routinely detectable even with the current state-of-the-art instrumentation. The best insight into terrestrial planet composition, therefore, is currently offered by Earth-sized ultra-short-period planets (USPs; R. Sanchis-Ojeda et al. 2014) whose RV semiamplitudes are typically an order of magnitude larger than their longer-period counterparts.

USPs ($R_p < 2\ R_\oplus$, $P_{orb} < 1$ days) are expected to be stripped rocky cores (R. Sanchis-Ojeda et al. 2014; M. S. Lundkvist et al. 2016), since they are so intensely irradiated by their host stars (>650 $S_\oplus$ around Sun-like stars; M. S. Lundkvist et al. 2016). This has been observationally confirmed via transmission and emission spectroscopy for several USPs (e.g., LHS 3844 b, GJ 1252 b, and GJ 367 b, L. Kreidberg et al. 2019; I. J. M. Crossfield et al. 2022; and M. Zhang et al. 2024, respectively). Precise mass and radius measurements of USPs therefore allow us to directly probe their compositions, with fewer unknown parameters than planets that may have a gaseous atmosphere. Still, nonnegligible volatile envelopes have been suggested to be present on larger ($\sim$1.5–2 $R_\oplus$) USPs, such as TOI-561 b (C. L. Brinkman et al. 2023) and 55 Cnc e (B.-O. Demory et al. 2016; A. Tsiaras et al. 2016; F. Dai et al. 2019), though there may be other reasons for their anomalously low densities. Earth-sized and smaller USPs may be less likely to retain secondary atmospheres because of their lower escape velocities. Precise composition constraints for such planets are paramount for informing the formation pathways of terrestrial planets. For example, confirming a more complete sample of Earth-sized and smaller exoplanets may verify the mass dependence of compositional outcomes during the final stages of the giant impact phase of planet formation (e.g., J. Scora et al. 2022).

In addition to being ideal for precise interior composition studies, USPs are especially promising targets for detailed observations of their surface characteristics with the James Webb Space Telescope (JWST). TOI-6324 b, confirmed in the present work, has one of the highest emission spectroscopy metrics (ESM = 25; E. M. R. Kempton et al. 2018), which is a proxy for the expected signal-to-noise ratio (SNR) of secondary eclipse measurements by JWST. It is one of the most similar in size to Earth, even among previously selected JWST targets. Measuring the phase offset, longitudinal temperature distribution (day–night temperature contrast), and albedo from the phase curve will reveal the presence or absence of a secondary atmosphere (e.g., B.-O. Demory et al. 2016; I. Angelo & R. Hu 2017; L. Kreidberg et al. 2019; R. Hu et al. 2024; M. Weiner Mansfield et al. 2024). Furthermore, USPs may be subject to significant deformation due to tidal interactions (F. Dai et al. 2024), and the phase curve may constrain the degree of tidal distortion (E. M. Price & L. A. Rogers 2020). Secondary eclipse emission spectra, in the absence of a secondary atmosphere, will constrain the dominant surface rock type of the planet (R. Hu et al. 2012; L. Kreidberg et al. 2019; E. A. Whittaker et al. 2022; M. Zhang et al. 2024).

In this work, we set out to confirm and further characterize TOI-6324 b. This Letter is organized as follows: we detail the properties of the host star TOI-6324 (TIC 372207328) in Section 2. We present our transit modeling, phase-curve modeling, and radius measurement of TOI-6324 b in Section 3 and our RV monitoring and mass measurement in Section 4. We discuss the interior composition and possible tidal deformation of TOI-6324 b in Section 5, along with prospective JWST observations. We conclude with a summary of our key findings in Section 6.

2. Host Star Properties

2.1. Spectroscopic Analysis

A spectrum of TOI-6324 (TIC 372207328; 2MASS J22032128+6729596; Gaia DR2 2220012421430629632) was obtained with the High Resolution Echelle Spectrometer (HIRES; S. S. Vogt et al. 2014) on the 10 m Keck I Telescope situated at Maunakea. The observation was taken on 2023 November 26 UT at 900 s exposure time, with a peak SNR of ∼150. We employed the `SpecMatch-Emp` routine (S. W. Yee et al. 2017) to empirically derive spectroscopic parameters by cross-matching the observed HIRES spectrum with an extensive library of well-calibrated stellar spectra observed by the California Planet Search collaboration. This routine mitigates the significant systematic effects found in direct spectral modeling of low-mass stars, such as poor continuum identification and normalization, or incomplete molecular line lists, which are especially troublesome for cool stars. From `SpecMatch-Emp` we find $T_{eff} = 3247 \pm 70$ K, consistent with the TESS Input Catalog (TIC; P. S. Muirhead et al. 2018; K. G. Stassun et al. 2018) estimate. We also find [Fe/H] = -0.32 ± 0.09, consistent with the estimate from J. A. Dittmann et al. (2016), and an upper limit on $v \sin i$ of <2 km s^{-1}.

Table 1
TOI-6324 System Parameters

Parameter	Symbol	Prior	Posterior (Median and 68.1% CI)
Stellar			
TIC ID	...	...	372207328
R.A. (hh:mm:ss)	α	...	22:03:22.69
Decl. (deg:arcmin:arcsec)	δ	...	+67:29:55.2
V (mag)	...	...	13.386 ± 0.026
K_s (mag)	...	...	8.691 ± 0.022
Effective Temperature (K)	$T_{\rm eff}$	...	3247 ± 70
Surface Gravity (cm s^{-2})	log g	...	4.93 ± 0.006
Iron Abundance (dex)	[Fe/H]	...	−0.32 ± 0.09
Rotational Broadening (km s^{-1})	$v \sin i$	...	<2
Stellar Mass ($M_\odot$)	$M_\star$	...	0.269 ± 0.012
Stellar Radius ($R_\odot$)	$R_\star$	...	0.293 ± 0.010
Stellar Density (g cm^{-3})	$\rho_\star$	...	10.7 ± 1.1
Limb Darkening q_1 (D. M. Kipping 2013)	...	U (0, 1)	0.40 ± 0.28
Limb Darkening q_2 (D. M. Kipping 2013)	...	U (0, 1)	$0.13^{+0.32}_{-0.13}$
Parallax (mas)[a]	π	...	48.6414 ± 0.0146
Distance (pc)[a]	d	...	20.5586 ± 0.0061
Planetary			
Emission Spectroscopy Metric	ESM	...	25
Equilibrium Temperature[b]	$T_{\rm eq}$	...	1216 ± 60
Planet/Star Radius Ratio	$R_{\rm p}/R_\star$	$\mathcal{N}\propto$ transit depth	0.0331 ± 0.0006
Time of Conjunction (BJD-2457000)	T_c	$\mathcal{N}$ (1738.5829, 10)	1739.97928 ± 0.00068
Impact Parameter	b	U (0, 1+$R_{\rm p}/R_\star$)	0.75 ± 0.03
Scaled Semimajor Axis	$a/R_\star$	...	3.17 ± 0.20
Orbital Inclination (deg)	i	...	74.6 ± 0.7
Orbital Eccentricity	e	0 (fixed)	0
Orbital Period (days)	$P_{\rm orb}$	$\mathcal{N}$ (0.279211, 10)	0.2792210 ± 0.00000010
Planetary Radius ($R_\oplus$)	$R_{\rm p}$	...	1.059 ± 0.041
RV Semiamplitude (m s^{-1})	K	Jeffreys (0.1, 30)	2.69 ± 0.51
Planetary Mass ($M_\oplus$)	$M_{\rm p}$	...	1.17 ± 0.22
KPF RV Jitter (m s^{-1})	$\sigma_{\rm jit,KPF}$	Jeffreys (0.1, 10)	1.31 ± 0.33
GP Kernel Amplitude (m s^{-1})	h	Jeffreys (0.1, 100)	$21.44^{+3.66}_{-2.81}$
GP Length (days)	l	Jeffreys (2P, $\sqrt{2}\tau$)	$1.76^{+0.29}_{-0.40}$

Notes.
[a] Gaia DR3.
[b] $T_{\rm eq}$ assumes a low albedo of $A_B = 0.1$.

We utilized the Python package `isoclassify` (D. Huber et al. 2017) to derive stellar parameters based on our derived spectroscopic stellar parameters and Gaia astrometry. `Isoclassify` directly computes the stellar radius ($R_\star$) using the Stefan–Boltzmann law, based on the observed K-band magnitude, Gaia parallax, and $T_{\rm eff}$. We adopted the MESA Isochrones and Stellar Tracks (J. Choi et al. 2016) and adhered to the default settings recommended by `isoclassify`. We compared our results with the empirical M dwarf mass–luminosity relation from A. W. Mann et al. (2019) and found that they are consistent within model uncertainties. The derived stellar parameters are given in the top section of Table 1.

2.2. Additional Companion Search

To validate transiting exoplanets and assess possible contamination of bound or unbound companions on the derived planetary radii (D. R. Ciardi et al. 2015), we observed TOI-6324 using near-infrared adaptive optics (AO) imaging and optical speckle imaging. The AO observations were conducted on 2023 August 5 UT using NIRC2 on Keck II as part of the K2 and TESS follow-up and validation survey by J. E. Schlieder et al. (2021). We utilized a three-point dither pattern. The narrow-angle mode provided a field of view of 10″ with a pixel scale of ∼0.″0099442 pixel^{-1}, using the narrow-band $K_{\rm cont}$ filter ($\lambda_o = 2.2706$; $\Delta\lambda = 0.0296$ μm).

Each frame had an integration time of 2.9 s, totaling 26.1 s on source. Flat fields were taken on sky, dark subtracted, and median averaged, and sky frames were created from the median average of dithered science frames. These were sky subtracted and flat fielded, resulting in a combined image with a resolution of 0.″053. Sensitivity was assessed by injecting simulated sources around the primary target at 20° intervals, scaling brightness until detection at 5σ significance (E. Furlan et al. 2017). We ruled out δmag <7 companions within 0.″5 (Figure 1).

In addition to high-contrast imaging, we investigated Gaia DR3 to search for stellar companions to TOI-6324. We identified no comoving sources in Gaia DR3 within a radius of 10″. We further assessed the astrometry of TOI-6324 for evidence of a stellar companion. The Gaia DR3 renormalized

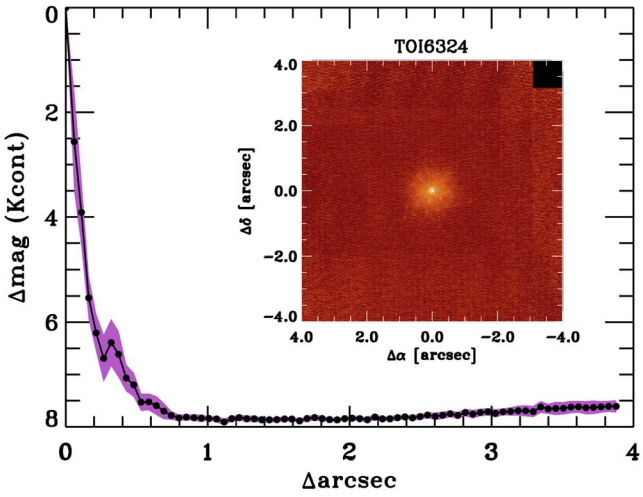

Figure 1. NIR AO imaging and sensitivity curve. The black points represent the 5σ detection limit, and the purple region represents the 1σ azimuthal dispersion of the contrast determination. Inset: AO image of TOI-6324 showing no evidence for a close-in companion.

unit weight error (RUWE) value represents the reduced χ^2 of Gaia's single-star astrometric solution and can be used to identify unresolved binaries (V. Belokurov et al. 2020) at separations of $\sim 0\farcs1$–$1\farcs0$ (M. L. Wood et al. 2021). For TOI-6324, RUWE = 1.165, well below the empirical threshold (RUWE = 1.4) at which binarity is likely.

2.3. Age

It is notoriously difficult to determine the age of M dwarfs using the methods applied to more massive stars. Their asteroseismic oscillations are too small to be detected with current capabilities (E. Rodríguez et al. 2016; Z. M. Berdiñas et al. 2017), and their isochrone ages are poorly calibrated (S. G. Engle & E. F. Guinan 2018). To assess the age of TOI-6324, we turned to gyrochronology (S. A. Barnes 2003, 2007), which relates the rotation rate of a star to its age based on empirically calibrated, mass-dependent spin-down rates (A. Skumanich 1972; S. A. Barnes 2007). However, we did not recover a robust rotation signal from a Lomb–Scargle periodogram (N. R. Lomb 1976; J. D. Scargle 1982) of TESS (G. R. Ricker et al. 2015) light curves (further described in Section 3) using a standard `lightkurve` routine (Lightkurve Collaboration et al. 2018). This may be attributed to the approximate upper limit of $P = 13.7$ days imposed by the length of the TESS orbit. Older stars with rotation periods longer than 13.7 days are difficult to age date using TESS photometry alone. E. R. Newton et al. (2016) also report a nondetection of the rotation period of TOI-6324, utilizing long-term photometric monitoring data from MEarth (Z. K. Berta et al. 2012; J. M. Irwin et al. 2015). Furthermore, using `BANYAN Σ` (J. Gagné et al. 2018), we found the Gaia DR3 kinematics of TOI-6324 are consistent with that of field stars. It is therefore unlikely that TOI-6324 is a member of any known nearby young moving groups. We are unable to derive a precise age estimate based on gyrochronology or by association, but it is likely that TOI-6324 is not a young ($\lesssim$100 Myr) star.

We calculated the probability that TOI-6324 is a member of the thick disk using the prescription of T. Bensby et al. (2014). TOI-6324 has a thick disk (TD)/thin disk (D) membership probability ratio TD/D = 84, i.e., it is likely a thick disk member based on its Galactic *UVW* velocity (U, V, W = 9.4 ± 1.0, −65.7 ± 2.1, −60.4 ± 0.5 km s^{-1}) after correcting for the local standard of rest (LSR). This is consistent with the trend that USPs tend to occur around older stars (S. P. Schmidt et al. 2024). We adopted the LSR as $U_\odot$, $V_\odot$, $W_\odot$ = 10.0 ± 1.0, 11.0 ± 2.0, 7.0 ± 0.5 km s^{-1} from J. Bland-Hawthorn & O. Gerhard (2016). Unfortunately, we do not have [α/Fe] data to back up the thick disk membership using the host star's abundances though we do find a nondetection of Hα emission in the HIRES spectrum (Section 2.1).

3. Photometric Analysis

3.1. Observations and Data

TOI-6324 was observed by TESS during Sectors 16, 17, 18, 24, 58, 77, and 78 (2019 September–November, 2020 April–May, 2022 November, and 2024 April–May). The data were processed by the TESS Science Processing Operations Center (SPOC at NASA Ames Research Center; J. M. Jenkins et al. 2016) and the MIT Quick-Look Pipeline (QLP; C. X. Huang et al. 2020). The transit signal of TOI-6324 b at 0.279 days was first alerted in a faint-star search in QLP, reported on the Exoplanet Follow-up Observing Program (ExoFOP[39]), and the SPOC pipeline detected the transit signature in every sector observed. We collected the 2 minute cadence SPOC light curves using the Python package `lightkurve` (Lightkurve Collaboration et al. 2018). We applied transit-depth bias correction to the Year 2 data (Sectors 16, 17, 18, and 24) that were affected by a sky background bias issue documented in the Sector 27 Data Release Notes. We utilized the Presearch Data Conditioning Simple Aperture Photometry (PDC-SAP) light curves (J. C. Smith et al. 2012; M. C. Stumpe et al. 2012, 2014; J. D. Twicken et al. 2010) for transit modeling after removing data points with nonzero data quality flags.

3.2. Transit Modeling

To prepare the PDC-SAP light curve for transit modeling, we first removed instrumental and long-term stellar systematics using the `wōtan` Python package (M. Hippke et al. 2019). We masked the transit signal of TOI-6324 b based on the QLP transit parameters. We then used an iterative sigma-clipping spline fit (`rspline`) with a width of 0.5 days to detrend the transit-masked light curve.

Our transit model was constructed using the `exoplanet` package (D. Foreman-Mackey et al. 2021a), a gradient-based probabilistic inference toolkit for modeling time-series astronomical data. We used the transit parameters reported by QLP (depth, duration, orbital period, and epoch) as the basis for uninformative priors (either uniform or broad normal distributions) to initialize our model. This allowed for a thorough and unconstrained search of the parameter space. We additionally imposed Gaussian stellar radius and density priors derived in this work (see Section 2 and Table 1). Limb-darkening coefficients q_1 and q_2 were reparameterized following the quadratic law formulation of D. M. Kipping (2013). We assumed a circular orbit ($e = 0$) for model simplicity. Since the orbital period is extremely short, we expect this to be a valid assumption due to tidal circularization. The transit model further included the planet-to-star radius ratio $R_p/R_\star$ derived

[39] https://exofop.ipac.caltech.edu/tess/target.php?id=372207328

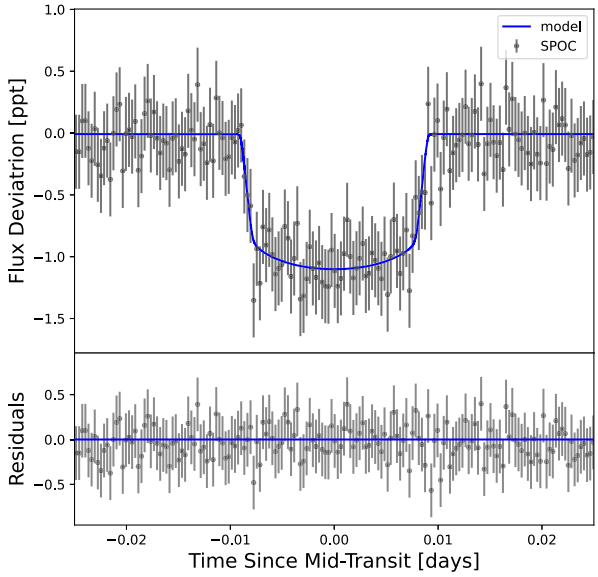

Figure 2. Binned and phase-folded SPOC PDC-SAP light curve of TOI-6324 revealing the transit signal of TOI-6324 b, with the best-fit transit model overplotted in blue. The residuals (data minus model) are shown in the bottom panel.

from transit depth, and the impact parameter b. The orbital inclination i was derived from b. We fit all transits assuming a constant period, since we did not identify any significant transit-timing variations.

A maximum a posteriori transit model solution was determined from an initial nonlinear optimization using `pyMC3` and set as the initial condition for sampling. We then explored the parameter space using No U-Turn Sampling (M. D. Hoffman & A. Gelman 2011) in a gradient-based Hamiltonian Monte Carlo (R. Neal 2011; M. Betancourt 2017) framework in `pyMC3` to generate the transit parameter posteriors. We ran two chains for 10,000 draws, with 5000 iterations to tune (15,000 steps total). We list the median values of the posterior distributions for the transit parameters in Table 1 along with the 68.3% confidence intervals. Figure 2 shows the binned and phase-folded PDC-SAP light curve of TOI-6324, with a robust detection of TOI-6324 b, along with the best-fit transit model. We report a radius of $R_{\rm p} = 1.059 \pm 0.041\ R_{\oplus}$ for TOI-6324 b based on the best-fit planet-to-star radius ratio $R_{\rm p}/R_{\star} = 0.0331 \pm 0.0006$ and our derived stellar radius of $R_{\star} = 0.293 \pm 0.010\ R_{\odot}$ (Table 1).

3.3. Additional Photometry Sources

In addition to the SPOC light curves, we obtained TESS-Gaia light curves (TGLC; T. Han & T. D. Brandt 2023), which are created from TESS Full Frame Images forward-modeled with the effective point-spread function to remove contamination from nearby stars. Based on Gaia DR3 positions and magnitudes, these light curves achieve a very high-treatment account of dilution. We performed an identical analysis on the TGLCs and find $R_{\rm p} = 1.075 \pm 0.05\ R_{\oplus}$ consistent with the result from the SPOC light curves within 1σ. Furthermore, TOI-6324 b was observed with the 200 inch Hale Telescope at Palomar Observatory for transit validation (J. Gomez Barrientos et al. 2024). The radius measurement of J. Gomez Barrientos et al. (2024), using both ground-based and TESS SPOC light curves, is consistent with the measurement from this work.

3.4. Additional Transiting Planet Search

No additional transiting planet candidates of TOI-6324 have been reported by QLP nor SPOC. To search for additional transit signals in the PDC-SAP light curves described in Section 3.2, we masked the transits of TOI-6324 b and performed a box-least-square (G. Kovács et al. 2002) analysis using the `lightcurve.to_periodogram` function of `lightkurve` (Lightkurve Collaboration et al. 2018). We allowed for periods between 0.1 and 30 days and transit durations between 0.1 and 2.15 hr. We phase-folded the light curve on the significant periodic signals from this search, and we did not identify any additional planetary transit signals.

3.5. Phase Curve

TOI-6324 b is ∼20% from the Roche limit, making it likely to be tidally distorted (see Section 5.3). We searched the TESS light curves for evidence of phase-curve variation and secondary eclipse signal from TOI-6324 b. The light curve was iteratively sigma-clipped and detrended in the same manner as in Section 3.2 but with a wider spline width of $2 * P_{\rm orb}$ or ∼13.4 hr to ensure any phase-curve signal was not removed in the detrending step. The light curve was then phase-folded and binned to ∼10 minute intervals (50 bins total). We used `batman` (L. Kreidberg 2015) to construct a secondary eclipse model based on the transit parameters derived in Section 3.2 (Table 1) but with the limb-darkening coefficients (q_1, q_2) set to 0. The eclipse time ($t_{\rm sec}$) was fixed to a 0.5 phase offset from the primary transit time.

In addition to the secondary eclipse, we modeled the out-of-eclipse phase-curve variation, initially characterized by a combination of the illumination effect from reflected stellar light ($A_{\rm ill}$), an offset of the peak illumination effect (θ), and ellipsoidal light variation (ELV; $A_{\rm ELV}$). $A_{\rm ill}$ was fixed to be the same as the secondary eclipse depth ($\delta_{\rm sec}$). We found that the TESS data do not have a sufficient SNR to robustly constrain θ, and thus, we set $\theta = 0$ for model simplicity.

The ellipsoidal light variation $A_{\rm ELV}$ can be due to both the tidal distortion of the star and the planet itself. We estimated that the stellar component is likely smaller than 1 ppm (e.g., S. Faigler et al. 2012); however, the planetary distortion can be substantial given the extremely short orbital period of the planet. We compared two phase-curve models: with and without the ellipsoidal light variation $A_{\rm ELV}$. Combined with the secondary eclipse model, the best-fit solutions were determined using the `Levenberg-Marquardt` least-squares likelihood maximization method (`lmfit`; M. Newville et al. 2014). We employed a nested sampling routine using `dynesty` (J. S. Speagle 2020; S. Koposov et al. 2024) to sample the posteriors and compare the Bayesian evidence ($\log(Z)$) of the two models and found that the non-ELV model is preferred over the ELV-inclusive model ($\Delta \log(Z) = 5$). We show in Figure 3(a) the best-fit phase-curve models with and without ELV. The posterior medians of the non-ELV and ELV models are consistent within 1σ uncertainties, and from the preferred non-ELV model, we find $\delta_{\rm sec} \equiv A_{\rm ill} = 42 \pm 28$ ppm ($<2\sigma$). From the ELV model, we report a tentative ($\sim 1\sigma$) detection of $A_{\rm ELV} = 21 \pm 17$ ppm, corresponding to a Bond albedo of $A_B = 0.36^{+0.28}_{-0.36}$ (Figure 3(b)).

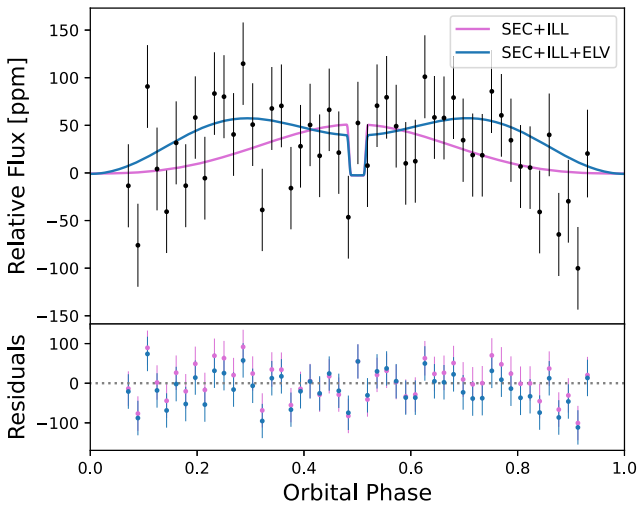

(a)

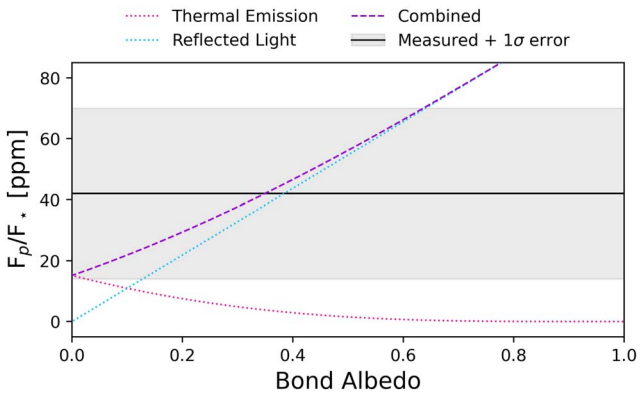

(b)

Figure 3. (a) Binned and phase-folded TESS light curve of TOI-6324. The pink curve shows the best-fit model without ellipsoidal light variation (ELV) in the phase-curve model, and the blue curve shows the best-fit result that includes the ELV term. The residuals (data minus model) from each model are shown in the bottom panel. (b) Thermal emission (pink dotted line) and reflected light (blue dotted line) in the TESS band as a function of the Bond albedo. The flux ratio ($F_p/F_\star$) measured in this work is shown as the black line with the associated 1σ confidence shaded in gray. The phase-curve variation observed in the TESS band is likely attributed to a combination of both thermal emission and reflected stellar light (purple dashed line).

4. Spectroscopic Analysis

4.1. Observations and Data

We obtained high-resolution spectra of TOI-6324 with the Keck Planet Finder (KPF; S. R. Gibson et al. 2016, PI: A. Howard) on Keck I. KPF is a high-resolution ($R \sim 98{,}000$), optical (445–870 nm), fiber-fed echelle spectrometer newly commissioned in late 2022. The confirmation of TOI-6324 b in this work is among the first science results of KPF. KPF boasts an internal instrumental RV precision of $\sim$50 cm s^{-1} and has demonstrated the capability to detect a 1.44 $M_\oplus$ USP to greater than 5σ precision (TOI-6255 b; F. Dai et al. 2024). We collected a total of 77 KPF spectra of TOI-6324 between 2023 June 30 UT and 2024 January 1 UT (see Table 2). Each exposure was 15 minutes, and the average SNR achieved was 65 at 550 nm. We aimed to obtain multiple exposures per night in order to mitigate some of the instrumental drift. The spectra

Table 2
Keck/KPF Radial Velocities of TOI-6324

Time (BJD)	RV (m s^{-1})	RV Uncertainty (m s^{-1})
2460126.076182692 [a]	−32.97	1.08
2460130.010714815 [a]	−48.53	1.25
2460135.004611146 [a]	−50.03	3.23
2460135.099483773 [a]	−37.17	1.70
2460146.114391493 [a]	−48.06	1.15
2460150.082071852 [a]	−20.9	1.12
2460153.098518762	−32.14	1.13
2460153.127477107	−37.35	1.23
2460159.95573294	−54.03	1.14
2460159.987071331	−52.14	1.13
2460162.964025116	−56.23	1.67
2460163.075380926	−54.04	1.63
2460169.969600474	−58.56	1.10
2460170.080126852	−52.53	1.16
2460176.841209965	−55.04	1.74
2460177.049994664	−53.08	1.72
2460180.875071331	−54.19	1.11
2460181.011329491	−51.37	1.13
2460182.876525359	−58.25	1.12
2460183.013670394	−59.47	1.09
2460183.980496354 [a]	−48.57	1.10
2460184.814127651	−96.50	1.06
2460184.914328611	−92.69	1.05
2460185.86687493	−84.08	1.22
2460185.935370845	−81.48	1.13
2460186.038032164	−80.85	1.21
2460187.792816146	−51.63	1.14
2460187.894425023	−48.05	1.23
2460188.019864653	−47.90	1.26
2460188.797937361	−40.15	1.18
2460188.825234838	−40.28	1.23
2460189.006935509	−37.43	1.30
2460189.962912512	−38.08	1.17
2460190.01121147	−39.69	1.22
2460190.05758022[a]	−33.78	1.13
2460192.812904292[a]	−42.71	1.16
2460196.778913785[a]	−56.79	1.17
2460196.813865821	−49.94	1.15
2460196.863170963	−48.97	1.19
2460197.766617256[a]	−70.66	1.65
2460197.793505319	−45.34	1.31
2460197.832056304	−50.06	1.14
2460198.802907853	−34.68	1.05
2460198.853179663	−38.10	1.09
2460198.877306925	−38.51	1.03
2460199.762083811	−53.57	1.19
2460199.801108737	−53.61	1.15
2460199.846550467	−53.37	1.15
2460200.760515219	−45.52	1.13
2460200.82617912	−45.10	1.40
2460200.856759512	−49.55	1.38
2460204.762007308	−62.63	1.16
2460204.793847212	−65.26	1.15
2460204.923963133	−61.56	1.24
2460208.770297217	−64.04	1.11
2460208.838113155	−62.98	1.20
2460208.867704152[a]	−53.37	1.16
2460209.752046775	−50.23	1.41
2460209.791566944	−50.48	1.16
2460209.82930193	−53.22	1.23
2460211.734217746	−39.43	1.07
2460211.84252483	−45.36	1.13
2460211.911891459	−40.03	1.14
2460252.886912332	−24.69	1.12

Table 2
(Continued)

Time (BJD)	RV ($m\,s^{-1}$)	RV Uncertainty ($m\,s^{-1}$)
2460252.94776194	−22.74	1.23
2460273.721432364	19.40	0.96
2460273.732485145	18.74	1.00
2460273.746181982	17.70	1.02
2460273.757201615	18.39	1.04
2460273.768154097	16.20	1.06
2460273.779157795	17.94	1.06
2460273.79369893	15.90	1.02
2460273.804679974	15.02	1.04
2460273.815668433	15.01	1.00
2460273.826684487	17.69	1.02
2460310.761742466	−88.81	1.09
2460310.791932109	−84.13	1.21

Note.
[a] Single-measurement nights and nightly 3σ outlier measurements excluded from our RV fits.

(This table is available in its entirety in machine-readable form in the online article.)

were reduced using the publicly accessible KPF Data Reduction Pipeline (DRP);[40] the RVs were extracted with the template matching code `serval` (M. Zechmeister et al. 2018) after minor modifications for KPF (F. Dai et al. 2024). RVs from nights with only a single measurement, as well as nightly 3σ outlier measurements, noted with a footnote in Table 2, were excluded, leaving 65 RV measurements taken over 23 nights for fitting.

4.2. Gaussian Process Model

To disentangle the planetary RV modulation from the significant instrumental noise in the RV variations of TOI-6324, we employed a Gaussian process (GP) regression model. We used the package `radvel` (B. J. Fulton et al. 2018) for this analysis. The correlated noise is likely a result of stochastic instrumental drift. Stellar pulsations that normally affect observations in more massive stars have very low amplitudes in M dwarfs, and because they occur on much shorter timescales, they are averaged out in each exposure (H. Kjeldsen & T. R. Bedding 1995; W. J. Chaplin et al. 2019). In our analysis of the light curves, we did not identify any periodic variations that could be attributed to rotationally modulated stellar activity or pulsations. As such, we used a squared-exponential GP kernel in our model, rather than the widely used quasiperiodic kernel (e.g., S. K. Grunblatt et al. 2015; V. Rajpaul et al. 2015; C. L. Brinkman et al. 2023), for model simplicity (F. Dai et al. 2019, 2021, 2024). This is included in the covariance matrix that is factored into the likelihood function. See F. Dai et al. (2024) for a detailed explanation of these expressions.

The model basis included the orbital elements of orbital period $P_{\rm orb}$, time of conjunction T_c, and RV semiamplitude K, and the eccentricity e and argument of pericenter ω were included jointly as $\sqrt{e}\cos\omega$ and $\sqrt{e}\sin\omega$. We imposed Gaussian priors on $P_{\rm orb}$ and T_c derived from our transit analysis (see Section 3 and Table 1). We placed a hard lower bound for the semiamplitude of $K > 0$, and we additionally imposed Jeffreys priors on the jitter term for KPF $\sigma_{\rm jit,KPF}$, as well as the GP hyperparameters of amplitude h and length l. We set a lower bound of $l > 1$ day to ensure the GP did not fit out the 6.7 hr planetary signal of TOI-6324 b. As in the transit model, we fixed the eccentricity to 0.

The standard `radvel` routine employs `emcee` (D. Foreman-Mackey et al. 2013) to explore the parameter space in a Markov Chain Monte Carlo (MCMC) framework. We ran 128 walkers for 10^4 runs in three ensembles for parallelization, achieving a maximum Gelman–Rubin statistic of 1.001. We show the best-fit GP model in panel (a) and the best-fit Keplerian solution for TOI-6324 b in panel (c) of Figure 4. The median values of the posterior distributions for the orbital parameters and GP hyperparameters are presented in Table 1, respectively. We found that the RV semiamplitude imposed by TOI-6324 b is robustly detected at 5σ precision with $K = 2.69 \pm 0.51\ m\,s^{-1}$. We did not detect any additional periodic signals or longer-term RV trends in this data set for evidence of another RV planet.

4.3. Floating Chunk Offset Method

To check if there was any overfitting from the GP analysis, we additionally performed a fit to the RVs using the floating chunk offset (FCO) method (e.g., A. P. Hatzes et al. 2010, 2011; A. P. Hatzes 2014). FCO is a common method for determining the RV semiamplitudes of USPs ($P \lesssim 1$ day), whose nightly RV variations are typically larger than individual RV measurement uncertainties (H. J. Deeg et al. 2023). By assigning nightly additive RV offsets to grouped observations, we focus entirely on intranight RV variations and effectively remove any long-term ($P > 1$ day) stellar and instrumental systematics.

As done for the GP fit, RVs from single-measurement nights and nightly 3σ outliers were excluded, noted with a footnote in Table 2. We assigned an offset term for each of 23 nights of observation, $\gamma_{\rm night}$. This model differs from the GP model in that we remove the squared-exponential kernel and use only the white noise component in the covariance function. We implicitly include nightly offsets in the measured RV values in the likelihood function. We again used `emcee` for sampling in an MCMC to explore the posteriors of the model, mirroring the procedure in our GP analysis. From the FCO method, we detected TOI-6324 b at 2σ precision, with a RV semiamplitude of $K = 2.19 \pm 1.02\ m\,s^{-1}$. This is consistent with the result of the GP model within 1σ uncertainties. Panel (d) of Figure 4 shows the Keplerian solution from the FCO model in phase with the GP model. Because the FCO model requires many more parameters (due to each $\gamma_{\rm night}$) than the GP model, therefore introducing larger uncertainty, we chose to adopt the GP model result for further analyses.

5. Discussion

5.1. Planet Composition

With precise mass and radius measurements (both $< 20\%$ uncertainties) of TOI-6324 b, we are able to approximate its interior composition. As mentioned, because USPs are so strongly irradiated by their host stars, it is suggested that any thick H/He envelopes should be stripped away (e.g., R. Sanchis-Ojeda et al. 2014; M. S. Lundkvist et al. 2016; L. Wang & F. Dai 2018; L. Kreidberg et al. 2019; M. Zhang et al. 2024), allowing for direct constraint of their compositions. To compare with other

[40] https://github.com/Keck-DataReductionPipelines/KPF-Pipeline

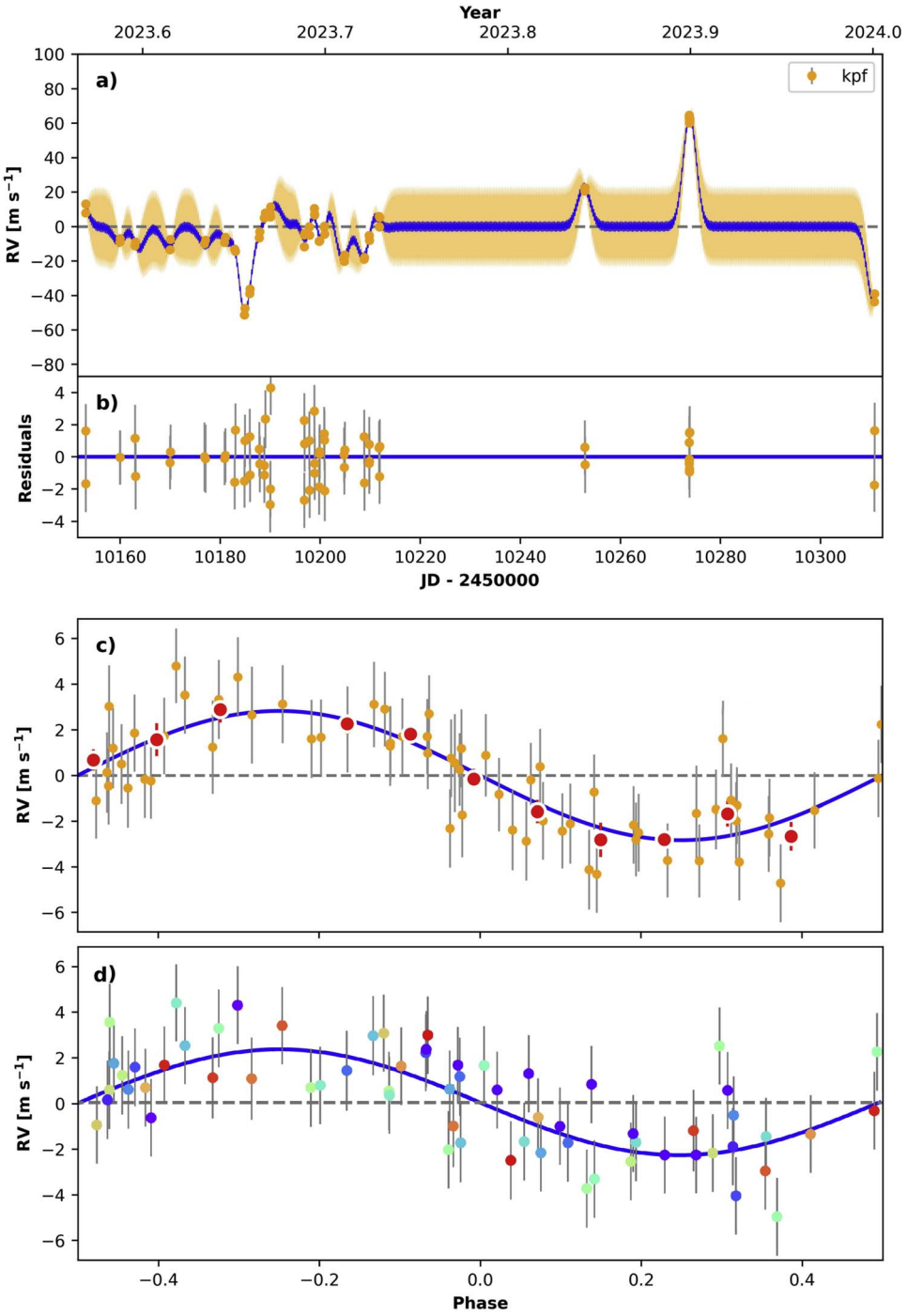

Figure 4. The radial velocity (RV) variations of TOI-6324 observed with KPF. (a) Time-series RV measurements along with the best-fit `radvel` Gaussian process (GP) model (blue line) used to remove stellar and instrumental systematics longer than the 6.7 hr orbital period of TOI-6324 b (see Section 4.2). The yellow contour represents the uncertainty of the GP model. Data points have been median-offset by −49.94 m s^{-1}; the raw values are given in Table 2. (b) Residuals (data–GP model). (c) RV variations of TOI-6324 as a function of orbital phase, resulting from our GP model. The red points show RVs binned to 10% of $P_{\rm orb}$. (d) RV variations of TOI-6324 as a function of orbital phase, resulting from our floating chunk offset (FCO) analysis (see Section 4.3). Data points are colored by observation date. The measured RV semiamplitude from both the GP and FCO analyses are consistent within 1σ ($K_{\rm GP} = 2.69 \pm 0.51$ m s^{-1} and $K_{\rm FCO} = 2.19 \pm 1.02$ m s^{-1}).

confirmed USPs (queried from the NASA Exoplanet Archive[41]) and Earth-sized planets, we plotted TOI-6324 b on a mass–radius diagram along with the model composition curves from L. Zeng et al. (2016), shown in Figure 5. The light purple colored points represent all confirmed $R_{\rm p} < 2\ R_{\oplus}$ planets with well-constrained masses and radii (<20% uncertainties), while the dark purple points highlight the USPs among these with $P < 1$ day. Similarly to other USPs, TOI-6324 b closely follows the Earth-like composition curve of 30% iron and 70% $MgSiO_3$ silicate rock.

5.2. Core Mass Fraction

To further characterize the interior composition of TOI-6324 b, we modeled the iron mass fraction (Fe-MF), which describes

[41] https://exoplanetarchive.ipac.caltech.edu

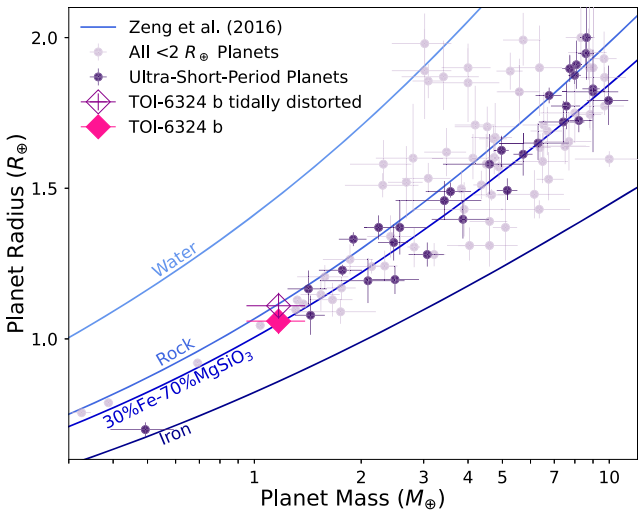

Figure 5. Mass–radius diagram of confirmed USPs (dark purple) and other rocky planets $<2\ R_\oplus$ (light purple). TOI-6324 b is plotted in pink. The magenta-outlined point represents TOI-6324 b in the case that it is tidally distorted by 5%. In the spherical case, $\mathrm{CMF}_{R_{\rm tran}} = 27\% \pm 37\%$, while in the distorted case, $\mathrm{CMF}_{R_{\rm vol}} = 3\% \pm 40\%$.

the fraction of the planet's mass that is comprised of the iron core. We modeled the core mass fraction (CMF) using `Manipulate Planet`,[42] a numerical tri-layer planetary interior model with an iron core, silicate rock mantle, and surface water layer (L. Zeng & D. Sasselov 2013; L. Zeng et al. 2016). The model assumes an undifferentiated core and numerically solves the interior structure of a planet based on the equation of state extrapolated from Earth's seismic density profile (using the preliminary reference earth model, A. M. Dziewonski & D. L. Anderson 1981). We adjusted the model to remove the water layer, and from this bi-layer iron and rock model, we found an Fe-MF (adopted as the CMF in this model) of $27\% \pm 37\%$ for TOI-6324 b.

We additionally employed a more sophisticated model, `exopie` (M. Plotnykov & D. Valencia 2024), based on SUPEREARTH (D. Valencia et al. 2006; M. Plotnykov & D. Valencia 2020), which computes an iron mass fraction Fe-MF, distinct from the general CMF. The Fe-MF calculation takes into account the iron that could be in the mantle and removes any light elements in the core, as well as different degrees of core differentiation. We assumed that there is a variable amount of Fe in the mantle and Si in the core (0%–20%) but set the Mg/Si ratio in the mantle to be Earth-like (∼0.9). Ni in the core was fixed to 10%. Using a Monte Carlo scheme, we found that TOI-6324 b has a CMF=$32\% \pm 19\%$ and Fe-MF = $30\% \pm 14\%$. These results are in agreement with the simpler model of L. Zeng et al. (2016).

5.3. Tidal Distortion

The extremely short (6.7 hr) orbit of TOI-6324 b gives rise to the possibility that it is substantially tidally distorted. Such an effect has been suggested for TOI-6255 b, a 1.079 $R_\oplus$ USP on a 5.7 hr orbit (F. Dai et al. 2024). Tidal distortion would have a nonnegligible effect on the volumetric radius $R_{\rm vol}$ and the effective transit radius of a planet and thus must be accounted for when approximating the bulk planet composition.

[42] https://lweb.cfa.harvard.edu/~lzeng/manipulateplanet.cdf

Following the method of F. Dai et al. (2024) we assess the degree of deformation due to tidal stress first by comparing the orbital period to the Roche limit of an incompressible fluid (S. Rappaport et al. 2013). The Earth is not very well modeled as an incompressible fluid, so this formula is a very rough approximation:

$$P_{\rm Roche} \approx 12.6\ {\rm hr} \left(\frac{\rho_{\rm p}}{1\ {\rm g\ cm^{-3}}}\right)^{-1/2}, \quad (1)$$

where $\rho_{\rm p}$ is the mean bulk density of the planet. The orbital period of the Roche limit, $P_{\rm Roche}$, is the minimum orbital period that a planet may attain before being tidally disrupted. At periods shorter than $P_{\rm Roche}$, tidal forces imposed by the host star become stronger than the self-gravity of the planet, and the planet begins to disintegrate. For TOI-6324 b, $P_{\rm Roche} = 5.41 \pm 0.15$ hr, bringing it close to the tidal disruption limit with $P_{\rm orb}/P_{\rm Roche} = 1.24 \pm 0.15$, though not extremely so. Still, only TOI-6255 b rivals TOI-6324 b in approaching the tidal disruption limit among confirmed USPs (see Figure 5 of F. Dai et al. 2024). The tidal decay timescale for TOI-6324 b, based on the star-to-planet mass ratio, mean stellar density, orbital period, and a nominal stellar tidal quality factor $Q_\star^{'} = 10^7$, is $\tau_P \approx 8$ Gyr. To reach the Roche limit, the orbital period would need to decrease by ∼20%, which would occur within $\tau_{\rm Roche} \approx 550$ Myr.

To estimate the tidal distortion $\delta R_{\rm p}$ of TOI-6324 b, we used the Love number h_2 for a solid homogeneous planet (A. E. H. Love 1944), which describes the radial tidal displacement of a planet's surface. h_2 depends on the mean tensile strength of the planetary material. For Earth, h_2 has been estimated to be 0.6–0.9 (K. Lambeck 1980). We adopted $h_2 = 1$ assuming a weaker material strength for USPs, as in F. Dai et al. (2024). This gives $\delta R_{\rm p} = 0.07$ for TOI-6324 b. A more robust detection of ellipsoidal light variation than we could recover in the TESS phase curve (Section 3.5, Figure 3(a)) would provide more conclusive evidence that TOI-6324 b is tidally deformed.

Since TOI-6324 b, like other USPs, is expected to be tidally locked (J. N. Winn et al. 2018), its planetary rotation period is the same as its orbital period of 6.7 hr. This may also lead to a nonnegligible rotational deformation. This is quantified by

$$q = \frac{\Omega^2 R_p^3}{G M_p}, \quad (2)$$

or the surface gravity acting against centrifugal forces at the planet's surface. We estimated $q = 0.04$ for TOI-6324 b. The deformation of the planet due to the combination of tidal bulge and rotational deformation results in an ellipsoidal shape with semimajor axes R_1 pointing toward the host star, R_2 pointing along the direction of orbital motion, and R_3 pointing along the planet's rotation axis (A. C. M. Correia et al. 2014). The total volumetric radius of the planet is defined as $R_{\rm vol} \equiv (R_1 R_2 R_3)^{1/3}$. During transit, a planet's transit radius is roughly $R_{\rm tran} \equiv (R_2 R_3)^{1/2}$, and the true volumetric radius is larger than the transit radius by $R_{\rm vol}/R_{\rm tran} = 1 + \frac{7}{12}\delta R_{\rm p}$ (F. Dai et al. 2024). We found $R_{\rm vol}/R_{\rm tran} = 1.05$, i.e., there is a 5% increase in the volumetric radius compared to the transit radius. The modeled CMF changes significantly from $\mathrm{CMF}_{R_{\rm tran}} = 27^{+37}_{-27}\%$ to $\mathrm{CMF}_{R_{\rm vol}} = 3\% \pm 40\%$, more consistent with a pure-rock composition. However, within

the large uncertainties, this qualitatively does not alter the results of Sections 5.1 and 5.2 (Figure 5).

5.4. JWST Prospects

USPs such as TOI-6324 b are particularly excellent targets for phase-curve and secondary eclipse observations with JWST. Several such systems have been selected or have already been successfully observed with JWST (e.g., 55 Cnc e, GJ 367 b, K2-141 b, LHS 3844 b, TOI-561 b, TOI-1685 b, TOI-2445 b, TOI-4481 b, and WASP-47 e). Precise study of their surfaces will revolutionize our understanding of planetary atmospheres and geology. USPs tend to orbit late-type stars (F. Dai et al. 2024), and thus their flux contrasts with their host stars are observationally favorable, on the order of 100 ppm in the infrared. We computed the ESM (E. M. R. Kempton et al. 2018) for TOI-6324 b to be 25. This is the highest ESM target among Earth-sized ($0.8\ R_\oplus < R_p < 1.2\ R_\oplus$) planets. The TESS data alone are insufficient for robustly constraining the phase-curve variation, though we do find preliminary evidence of several tens of parts per million in the optical ($A_{\rm ill} = 42 \pm 28$ ppm and $A_{\rm ELV} = 21 \pm 17$ ppm; Section 3.5, Figure 3(a)). For USPs, the planet-to-star flux ratio is expected to be much more significant in the mid-IR (F. Dai et al. 2024). In the MIRI/low-resolution spectroscopy bandpass (5–12 μm), the planet's thermal emission increases to ∼280 ppm, assuming a low Bond albedo. We aim to include more detailed modeling of the TESS phase-curve variation in a future paper with comparison to JWST observations.

There are several scientific avenues for detailed characterization of TOI-6324 b with JWST MIRI/LRS (S. Kendrew et al. 2015) observations. Since USPs are tidally locked, they will have constant daysides and nightsides, resulting in significant longitudinal temperature contrasts across their surfaces. An observed offset in the phase curve would signify heat recirculation over the surface of the planet due to the presence of an outgassed secondary atmosphere (e.g., H. A. Knutson et al. 2009; B.-O. Demory et al. 2013; A. P. Showman et al. 2015; P. von Paris et al. 2016; I. Angelo & R. Hu 2017). A lack of phase offset indicates a bare rock surface (e.g., M. Zhang et al. 2024; M. Weiner Mansfield et al. 2024). In this case, variations in the phase curve will trace the projected shape of the planet across its orbit and help to constrain the extent of tidal distortion and provide key insights into the tidal interactions USPs undergo with their host stars (see Section 5.3; F. Dai et al. 2024).

For a bare rock surface, the emission spectrum will constrain the dominant surface rock type of the planet (R. Hu et al. 2012; L. Kreidberg et al. 2019; E. A. Whittaker et al. 2022; M. Zhang et al. 2024). The approximate equilibrium temperature of TOI-6324 b is $T_{\rm eq} = 1216 \pm 60$ K (Table 1), assuming a low albedo of 0.1. This is below the zero-pressure melting point of common silicates found on Earth (such as peridotite at 1390 K), and thus it is unlikely that TOI-6324 b has a pure lava surface, although the hotter dayside, which receives constant irradiation, may be partially molten. Assuming zero albedo, the temperature at the substellar point would be approximately 1824 K, which is sufficient to melt silicates. Excessive tidal heating may also contribute to violent volcanism at the surface (B. Jackson et al. 2008; R. Hu et al. 2012), if the planet actually has a nonzero eccentricity, contrary to our assumption in Section 3.2. Detection of basaltic or ultramafic surface mineralogy, based on the Si-O absorption feature from 8 to 10 μm, will constrain the ongoing geologic processes. Ultramafic rock is formed from high-temperature volcanism and has strong Si-O features, while basaltic rock is formed from Earth-like extrusive volcanism and typically exhibits weaker Si-O features. The presence of granitoid rock (the primary component of Earth's continental crust) is unlikely at the extreme temperatures of TOI-6324 b, which are high enough to melt feldspar and quartz (the primary minerals in granite). Dedicated simulations of these observations and effects will be included in future works.

6. Summary

In summary, we report the confirmation of TOI-6324 b using TESS transit observations and RV monitoring with KPF. The key findings are as follows:

1. TOI-6324 b has a transit radius of $1.059 \pm 0.041\ R_\oplus$. This is one of the closest to Earth-sized USPs confirmed to date and one of the only Earth-sized USPs with a precise mass measurement.
2. TOI-6324 b has a mass of $1.17 \pm 0.22\ M_\oplus$. The RV mass constraints from both GP regression and FCO methods are consistent within 1σ.
3. The 27% ± 37% CMF of TOI-6324 b, as with other $\gtrsim 1\ R_\oplus$ USPs, is consistent with an Earth-like composition.
4. Accounting for tidal distortion due to its short orbit ($P_{\rm orb}/P_{\rm Roche} = 1.24 \pm 0.15$), the radius may be inflated by ∼5%. This would alter the CMF to 3% ± 40%.
5. We report preliminary evidence of phase-curve variation ($A_{\rm ill} = 42 \pm 28$ ppm) from the TESS data. With an ESM of 25, TOI-6324 b is among the most favorable USP targets for JWST phase-curve and emission spectrum observations to constrain its surface mineralogy and tidal deformation.

Acknowledgments

The authors wish to recognize and acknowledge the very significant cultural role and reverence that the summit of Maunakea has always had within the indigenous Hawaiian community. We are most fortunate to have the opportunity to conduct observations from this mountain.

R.A.L. acknowledges this material is based upon work supported by the National Science Foundation Graduate Research Fellowship Program under grant No. 1842402 and grant No. 2236415. Any opinions, findings, and conclusions or recommendations expressed in this material are those of the author(s) and do not necessarily reflect the views of the National Science Foundation.

We thank Ellen Price for helpful discussions about tidal distortion.

A NASA Key Strategic Mission Support titled "Pinning Down Masses of JWST Ultra-short-period Planets with KPF" (PI: F. Dai) provided the telescope access and funding for the completion of this project.

This work was supported by a NASA Keck PI Data Award, administered by the NASA Exoplanet Science Institute. Data presented herein were obtained at the W. M. Keck Observatory from telescope time allocated to the National Aeronautics and Space Administration through the agency's scientific partnership with the California Institute of Technology and the University of California. The Observatory was made possible

by the generous financial support of the W. M. Keck Foundation.

D.R.C. acknowledges partial support from NASA Grant 18-2XRP18_2-0007.

J.M.J.O. acknowledges support from NASA through the NASA Hubble Fellowship grant HST-HF2-51517.001, awarded by STScI. STScI is operated by the Association of Universities for Research in Astronomy, Incorporated, under NASA contract NAS5-26555.

L.M.W. acknowledges support from the NASA Exoplanet Research Program (grant No. 80NSSC23K0269).

N.S. acknowledges support by the National Science Foundation Graduate Research Fellowship Program under grant Nos. 1842402 and 2236415 and the National Aeronautics and Space Administration (80NSSC21K0652).

This research was carried out in part at the Jet Propulsion Laboratory, California Institute of Technology, under a contract with the National Aeronautics and Space Administration (80NM0018D0004).

This research was carried out, in part, at the Jet Propulsion Laboratory and the California Institute of Technology under a contract with the National Aeronautics and Space Administration and funded through the President's and Director's Research & Development Fund Program.

This research has made use of the Exoplanet Follow-up Observation Program (NexScI 2022) website, which is operated by the California Institute of Technology, under contract with the National Aeronautics and Space Administration under the Exoplanet Exploration Program.

We acknowledge the use of public TESS data from pipelines at the TESS Science Office and at the TESS Science Processing Operations Center. Resources supporting this work were provided by the NASA HighEnd Computing (HEC) Program through the NASA Advanced Supercomputing (NAS) Division at Ames Research Center for the production of the SPOC data products.

This Letter made use of data collected by the TESS mission and are publicly available from the Mikulski Archive for Space Telescopes (MAST) operated by the Space Telescope Science Institute (STScI). Funding for the TESS mission is provided by NASA's Science Mission Directorate. K.A.C. and C.N.W. acknowledge support from the TESS mission via subaward s3449 from MIT.

Some of the data presented herein were obtained at Keck Observatory, which is a private 501(c)3 non-profit organization operated as a scientific partnership among the California Institute of Technology, the University of California, and the National Aeronautics and Space Administration. The Observatory was made possible by the generous financial support of the W. M. Keck Foundation.

Data: All the TESS data used in this Letter can be found in MAST (MAST Team 2021). This work uses data supplied from the NASA Exoplanet Archive (ExoFOP 2019).

Facility: Keck I/KPF, Keck I/HIRES, Keck II/NIRC2, TESS.

Software: `arviz` (R. Kumar et al. 2019), `astropy` (Astropy Collaboration et al. 2013, 2018), `batman` (L. Kreidberg 2015), `dynesty` (J. S. Speagle 2020; S. Koposov et al. 2024), `emcee` (D. Foreman-Mackey et al. 2013), `exopie` (M. Plotnykov & D. Valencia 2024), `exoplanet` (D. Foreman-Mackey et al. 2021b, 2024), `isoclassify` (D. Huber et al. 2017), `Lightkurve` (Lightkurve Collaboration et al. 2018), `lmfit` (M. Newville et al. 2014), `Manipulate Planet` (L. Zeng & D. Sasselov 2013; L. Zeng et al. 2016), MESA Isochrones and Stellar Tracks (MIST; J. Choi et al. 2016), `pyMC3` (J. Salvatier et al. 2016), `radvel` (B. J. Fulton et al. 2018), `SpecMatch-Emp` (S. W. Yee et al. 2017), `starry` (R. Luger et al. 2019), SUPEREARTH (D. Valencia et al. 2006), `theano` (Theano Development Team et al. 2016), `wōtan` (M. Hippke et al. 2019).

ORCID iDs

Rena A. Lee https://orcid.org/0000-0001-7058-4134
Fei Dai https://orcid.org/0000-0002-8958-0683
Andrew W. Howard https://orcid.org/0000-0001-8638-0320
Samuel Halverson https://orcid.org/0000-0003-1312-9391
Jonathan Gomez Barrientos https://orcid.org/0000-0002-0672-9658
Michael Greklek-McKeon https://orcid.org/0000-0002-0371-1647
Heather A. Knutson https://orcid.org/0000-0002-5375-4725
Benjamin J. Fulton https://orcid.org/0000-0003-3504-5316
Guðmundur Stefánsson https://orcid.org/0000-0001-7409-5688
Jack Lubin https://orcid.org/0000-0001-8342-7736
Howard Isaacson https://orcid.org/0000-0002-0531-1073
Casey L. Brinkman https://orcid.org/0000-0002-4480-310X
Nicholas Saunders https://orcid.org/0000-0003-2657-3889
Daniel Hey https://orcid.org/0000-0003-3244-5357
Daniel Huber https://orcid.org/0000-0001-8832-4488
Lauren M. Weiss https://orcid.org/0000-0002-3725-3058
Leslie A. Rogers https://orcid.org/0000-0003-0638-3455
Diana Valencia https://orcid.org/0000-0003-3993-4030
Mykhaylo Plotnykov https://orcid.org/0000-0002-9479-2744
Kimberly Paragas https://orcid.org/0000-0003-0062-1168
Renyu Hu https://orcid.org/0000-0003-2215-8485
Te Han https://orcid.org/0000-0002-7127-7643
Erik A. Petigura https://orcid.org/0000-0003-0967-2893
Ryan Rubenzahl https://orcid.org/0000-0003-3856-3143
David R. Ciardi https://orcid.org/0000-0002-5741-3047
Aaron Householder https://orcid.org/0000-0002-5812-3236
Gregory J. Gilbert https://orcid.org/0000-0003-0742-1660
J. M. Joel Ong https://orcid.org/0000-0001-7664-648X
Jingwen Zhang https://orcid.org/0000-0002-2696-2406
Luke Handley https://orcid.org/0000-0002-9305-5101
Corey Beard https://orcid.org/0000-0001-7708-2364
Steven Giacalone https://orcid.org/0000-0002-8965-3969
Rae Holcomb https://orcid.org/0000-0002-5034-9476
Judah Van Zandt https://orcid.org/0000-0002-4290-6826
Ashley D. Baker https://orcid.org/0000-0002-6525-7013
Max Brodheim https://orcid.org/0009-0008-9808-0411
David Charbonneau https://orcid.org/0000-0002-9003-484X
Karen A. Collins https://orcid.org/0000-0001-6588-9574
Ian J. M. Crossfield https://orcid.org/0000-0002-1835-1891
William Deich https://orcid.org/0009-0000-3624-1330
Xavier Dumusque https://orcid.org/0000-0002-9332-2011
Steven R. Gibson https://orcid.org/0009-0004-4454-6053
Emily Gilbert https://orcid.org/0000-0002-0388-8004
Grant M. Hill https://orcid.org/0000-0002-7648-9119
Bradford Holden https://orcid.org/0000-0002-6153-3076
Jon M. Jenkins https://orcid.org/0000-0002-4715-9460
Russ R. Laher https://orcid.org/0000-0003-2451-5482
Kyle Lanclos https://orcid.org/0009-0004-0592-1850
W. Garett Levine https://orcid.org/0000-0002-1422-4430
Joel Payne https://orcid.org/0009-0008-4293-0341
Alex S. Polanski https://orcid.org/0000-0001-7047-8681

John O'Meara https://orcid.org/0000-0002-7893-1054
George R. Ricker https://orcid.org/0000-0003-2058-6662
Paul Robertson https://orcid.org/0000-0003-0149-9678
Arpita Roy https://orcid.org/0000-0001-8127-5775
Joshua E. Schlieder https://orcid.org/0000-0001-5347-7062
Christian Schwab https://orcid.org/0000-0002-4046-987X
Sara Seager https://orcid.org/0000-0002-6892-6948
Abby P. Shaum https://orcid.org/0000-0003-3133-6837
Martin M. Sirk https://orcid.org/0009-0007-8555-8060
Stephanie Striegel https://orcid.org/0009-0008-5145-0446
Johanna Teske https://orcid.org/0009-0008-2801-5040
Roland Vanderspek https://orcid.org/0000-0001-6763-6562
Gautam Vasisht https://orcid.org/0000-0002-1871-6264
Josh Walawender https://orcid.org/0000-0002-6092-8295
Sharon Xuesong Wang https://orcid.org/0000-0002-6937-9034
Joshua N. Winn https://orcid.org/0000-0002-4265-047X
Sherry Yeh https://orcid.org/0000-0002-4037-3114

References

Angelo, I., & Hu, R. 2017, AJ, 154, 232
Astropy Collaboration, Price-Whelan, A. M., Sipőcz, B. M., et al. 2018, AJ, 156, 123
Astropy Collaboration, Robitaille, T. P., Tollerud, E. J., et al. 2013, A&A, 558, A33
Barnes, S. A. 2003, ApJ, 586, 464
Barnes, S. A. 2007, ApJ, 669, 1167
Belokurov, V., Penoyre, Z., Oh, S., et al. 2020, MNRAS, 496, 1922
Bensby, T., Feltzing, S., & Oey, M. S. 2014, A&A, 562, A71
Berdiñas, Z. M., Rodríguez-López, C., Amado, P. J., et al. 2017, MNRAS, 469, 4268
Berta, Z. K., Irwin, J., Charbonneau, D., Burke, C. J., & Falco, E. E. 2012, AJ, 144, 145
Betancourt, M. 2017, arXiv:1701.02434
Bland-Hawthorn, J., & Gerhard, O. 2016, ARA&A, 54, 529
Brinkman, C. L., Weiss, L. M., Dai, F., et al. 2023, AJ, 165, 88
Chaplin, W. J., Cegla, H. M., Watson, C. A., Davies, G. R., & Ball, W. H. 2019, AJ, 157, 163
Choi, J., Dotter, A., Conroy, C., et al. 2016, ApJ, 823, 102
Ciardi, D. R., Beichman, C. A., Horch, E. P., & Howell, S. B. 2015, ApJ, 805, 16
Correia, A. C. M., Boué, G., Laskar, J., & Rodríguez, A. 2014, A&A, 571, A50
Crossfield, I. J. M., Malik, M., Hill, M. L., et al. 2022, ApJL, 937, L17
Dai, F., Howard, A. W., Batalha, N. M., et al. 2021, AJ, 162, 62
Dai, F., Howard, A. W., Halverson, S., et al. 2024, AJ, 168, 101
Dai, F., Masuda, K., Winn, J. N., & Zeng, L. 2019, ApJ, 883, 79
Deeg, H. J., Georgieva, I. Y., Nowak, G., et al. 2023, A&A, 677, A12
Demory, B.-O., de Wit, J., Lewis, N., et al. 2013, ApJL, 776, L25
Demory, B.-O., Gillon, M., de Wit, J., et al. 2016, Natur, 532, 207
Dittmann, J. A., Irwin, J. M., Charbonneau, D., & Newton, E. R. 2016, ApJ, 818, 153
Dziewonski, A. M., & Anderson, D. L. 1981, PEPI, 25, 297
Engle, S. G., & Guinan, E. F. 2018, RNAAS, 2, 34
ExoFOP 2019, Exoplanet Follow-up Observing Program - TESS, IPAC, doi:10.26134/EXOFOP3
Faigler, S., Mazeh, T., Quinn, S. N., Latham, D. W., & Tal-Or, L. 2012, ApJ, 746, 185
Foreman-Mackey, D., Hogg, D. W., Lang, D., & Goodman, J. 2013, PASP, 125, 306
Foreman-Mackey, D., Luger, R., Agol, E., et al. 2021a, JOSS, 6, 3285
Foreman-Mackey, D., Luger, R., Agol, E., et al. 2021b, JOSS, 6, 3285
Foreman-Mackey, D., Savel, A., Luger, R., et al. 2024, exoplanet: Gradient-based probabilistic inference for exoplanet data & other astronomical time series, v0.5.1, Zenodo, doi:10.5281/zenodo.1998447
Fulton, B. J., Petigura, E. A., Blunt, S., & Sinukoff, E. 2018, PASP, 130, 044504
Furlan, E., Ciardi, D. R., Everett, M. E., et al. 2017, AJ, 153, 71
Gagné, J., Mamajek, E. E., Malo, L., et al. 2018, ApJ, 856, 23
Gibson, S. R., Howard, A. W., Marcy, G. W., et al. 2016, Proc. SPIE, 9908, 990870
Gomez Barrientos, J., Greklek-McKeon, M., Knutson, H., & Giacalone, S. 2024, AAS/Division for Extreme Solar Systems Abstracts, 56, 600.10
Grunblatt, S. K., Howard, A. W., & Haywood, R. D. 2015, ApJ, 808, 127
Han, T., & Brandt, T. D. 2023, AJ, 165, 71
Hatzes, A. P. 2014, A&A, 568, A84
Hatzes, A. P., Dvorak, R., Wuchterl, G., et al. 2010, A&A, 520, A93
Hatzes, A. P., Fridlund, M., Nachmani, G., et al. 2011, ApJ, 743, 75
Hippke, M., David, T. J., Mulders, G. D., & Heller, R. 2019, AJ, 158, 143
Hoffman, M. D., & Gelman, A. 2011, arXiv:1111.4246
Hu, R., Bello-Arufe, A., Zhang, M., et al. 2024, Natur, 630, 609
Hu, R., Ehlmann, B. L., & Seager, S. 2012, ApJ, 752, 7
Huang, C. X., Vanderburg, A., Pál, A., et al. 2020, RNAAS, 4, 204
Huber, D., Zinn, J., Bojsen-Hansen, M., et al. 2017, ApJ, 844, 102
Irwin, J. M., Berta-Thompson, Z. K., Charbonneau, D., et al. 2015, in Cambridge Workshop on Cool Stars, Stellar Systems, and the Sun, 18th Cambridge Workshop on Cool Stars, Stellar Systems, and the Sun, 18, ed. G. T. van Belle & H. C. Harris (Flagstaff, AZ: Lowell Observatory), 767
Jackson, B., Barnes, R., & Greenberg, R. 2008, MNRAS, 391, 237
Jenkins, J. M., Twicken, J. D., McCauliff, S., et al. 2016, Proc. SPIE, 9913, 99133E
Kempton, E. M. R., Bean, J. L., Louie, D. R., et al. 2018, PASP, 130, 114401
Kendrew, S., Scheithauer, S., Bouchet, P., et al. 2015, PASP, 127, 623
Kipping, D. M. 2013, MNRAS, 435, 2152
Kjeldsen, H., & Bedding, T. R. 1995, A&A, 293, 87
Knutson, H. A., Charbonneau, D., Cowan, N. B., et al. 2009, ApJ, 690, 822
Koposov, S., Speagle, J., Barbary, K., et al. 2024, joshspeagle/dynesty: v2.1.4, Zenodo, doi:10.5281/zenodo.12537467
Kovács, G., Zucker, S., & Mazeh, T. 2002, A&A, 391, 369
Kreidberg, L. 2015, PASP, 127, 1161
Kreidberg, L., Koll, D. D. B., Morley, C., et al. 2019, Natur, 573, 87
Kumar, R., Carroll, C., Hartikainen, A., & Martin, O. A. 2019, JOSS, 4, 1143
Lambeck, K. 1980, The Earth's Variable Rotation: Geophysical Causes and Consequences (Cambridge: Cambridge Univ. Press)
Lightkurve Collaboration, Cardoso, J. V. D. M., Hedges, C., et al. 2018, Lightkurve: Kepler and TESS time series analysis in Python, v2.5.0, Astrophysics Source Code Library, ascl:1812.013
Lomb, N. R. 1976, Ap&SS, 39, 447
Love, A. E. H. 1944, A Treatise on the Mathematical Theory of Elasticity (4th ed.; New York: Dover Publications)
Luger, R., Agol, E., Foreman-Mackey, D., et al. 2019, AJ, 157, 64
Lundkvist, M. S., Kjeldsen, H., Albrecht, S., et al. 2016, NatCo, 7, 11201
Mann, A. W., Dupuy, T., Kraus, A. L., et al. 2019, ApJ, 871, 63
MAST Team 2021, TESS Light Curves - All Sectors, STScI/MAST, doi:10.17909/t9-nmc8-f686
Muirhead, P. S., Dressing, C. D., Mann, A. W., et al. 2018, AJ, 155, 180
Neal, R. 2011, in Handbook of Markov Chain Monte Carlo, ed. S. Brooks et al. (London: Chapman & Hall), 113
NexScI 2022, Exoplanet Follow-up Observing Program Web Service, IPAC, doi:10.26134/EXOFOP5
Newton, E. R., Irwin, J., Charbonneau, D., et al. 2016, ApJ, 821, 93
Newville, M., Stensitzki, T., Allen, D. B., & Ingargiola, A. 2014, LMFIT: Non-Linear Least-Square Minimization and Curve-Fitting for Python, v0.8.0, Zenodo, doi:10.5281/zenodo.11813
Plotnykov, M., & Valencia, D. 2020, MNRAS, 499, 932
Plotnykov, M., & Valencia, D. 2024, MNRAS, 530, 3488
Price, E. M., & Rogers, L. A. 2020, ApJ, 894, 8
Rajpaul, V., Aigrain, S., Osborne, M. A., Reece, S., & Roberts, S. 2015, MNRAS, 452, 2269
Rappaport, S., Sanchis-Ojeda, R., Rogers, L. A., Levine, A., & Winn, J. N. 2013, ApJL, 773, L15
Ricker, G. R., Winn, J. N., Vanderspek, R., et al. 2015, JATIS, 1, 014003
Rodríguez, E., Rodríguez-López, C., López-González, M. J., et al. 2016, MNRAS, 457, 1851
Salvatier, J., Wiecki, T. V., & Fonnesbeck, C. 2016, PeerJ Computer Science, 2, e55
Sanchis-Ojeda, R., Rappaport, S., Winn, J. N., et al. 2014, ApJ, 787, 47
Scargle, J. D. 1982, ApJ, 263, 835
Schlieder, J. E., Gonzales, E. J., Ciardi, D. R., et al. 2021, FrASS, 8, 63
Schmidt, S. P., Schlaufman, K. C., & Hamer, J. H. 2024, AJ, 168, 109
Scora, J., Valencia, D., Morbidelli, A., & Jacobson, S. 2022, ApJ, 940, 144
Showman, A. P., Lewis, N. K., & Fortney, J. J. 2015, ApJ, 801, 95
Skumanich, A. 1972, ApJ, 171, 565
Smith, J. C., Stumpe, M. C., Van Cleve, J. E., et al. 2012, PASP, 124, 1000
Speagle, J. S. 2020, MNRAS, 493, 3132
Stassun, K. G., Oelkers, R. J., Pepper, J., et al. 2018, AJ, 156, 102
Stumpe, M. C., Smith, J. C., Catanzarite, J. H., et al. 2014, PASP, 126, 100

Stumpe, M. C., Smith, J. C., Van Cleve, J. E., et al. 2012, PASP, 124, 985
Theano Development Team, Al-Rfou, R., & Alain, G. 2016, arXiv:1605.02688
Tsiaras, A., Rocchetto, M., Waldmann, I. P., et al. 2016, ApJ, 820, 99
Twicken, J. D., Clarke, B. D., Bryson, S. T., et al. 2010, Proc. SPIE, 7740, 774023
Valencia, D., O'Connell, R. J., & Sasselov, D. 2006, Icar, 181, 545
Vogt, S. S., Radovan, M., Kibrick, R., et al. 2014, PASP, 126, 359
von Paris, P., Gratier, P., Bordé, P., & Selsis, F. 2016, A&A, 587, A149
Wang, L., & Dai, F. 2018, ApJ, 860, 175
Weiner Mansfield, M., Xue, Q., Zhang, M., et al. 2024, ApJL, 975, L22
Whittaker, E. A., Malik, M., Ih, J., et al. 2022, AJ, 164, 258
Winn, J. N., Sanchis-Ojeda, R., & Rappaport, S. 2018, NewAR, 83, 37
Wood, M. L., Mann, A. W., & Kraus, A. L. 2021, AJ, 162, 128
Yee, S. W., Petigura, E. A., & von Braun, K. 2017, ApJ, 836, 77
Zechmeister, M., Reiners, A., Amado, P. J., et al. 2018, A&A, 609, A12
Zeng, L., & Sasselov, D. 2013, PASP, 125, 227
Zeng, L., Sasselov, D. D., & Jacobsen, S. B. 2016, ApJ, 819, 127
Zhang, M., Hu, R., Inglis, J., et al. 2024, ApJL, 961, L44